$LaPdIn_2$ with $MgCuAl_2$ and $REPdIn_2$ (RE = Y, Pr, Nd, Sm, Gd−Tm, Lu) with $HfNiGa_2$-Type Structure: Synthesis, Structure, and Physical Properties

Vasyl' I. Zaremba[†]

Inorganic Chemistry Department, Ivan Franko National University, Kyryla and Mephodiya Street 6, 79005 Lviv, Ukraine

Dariusz Kaczorowski[‡]

Institute of Low Temperature and Structure Research, Polish Academy of Sciences, P.O. Box 1410, 50-950 Wroclaw, Poland

Ute Ch. Rodewald, Rolf-Dieter Hoffmann, and Rainer Pöttgen*

Institut für Anorganische und Analytische Chemie, Universität Münster, Wilhelm-Klemm-Strasse 8, D-48149 Münster, Germany

Received October 9, 2003. Revised Manuscript Received November 10, 2003

New indides $REPdIn_2$ (RE = Y, La, Pr, Nd, Sm, Gd−Tm, Lu) have been synthesized from the elements by arc-melting. The indides with Y, Pr, Nd, Sm, Gd−Tm, and Lu as the rare earth metal component have been obtained in pure form by annealing the arc-melted samples in tantalum containers. Single crystals of $LaPdIn_2$ were obtained by recrystallization of a $LaPdIn_2$ sample from an indium flux. $LaPdIn_2$ crystallizes with the $MgCuAl_2$ structure: *Cmcm*, $a = 463.79(7)$ pm, $b = 1074.3(2)$ pm, $c = 746.4(2)$ pm, wR2 = 0.1149, 380 F^2 values, and 16 variables. The structure may be described as a palladium-filled $LaIn_2$ substructure. The latter is a strongly distorted $CaIn_2$-like arrangement. Together, the palladium and indium atoms build a three-dimensional $[PdIn_2]$ network in which the lanthanum atoms fill distorted pentagonal channels. The other $REPdIn_2$ indides crystallize with the $HfNiGa_2$ type, space group *I*4*mm*. Single crystals have been obtained for three compounds: $a = 1397.7(1)$ pm, $c = 925.5(1)$ pm, wR2 = 0.0662, 2098 F^2 values, 64 variables for $PrPdIn_2$; $a = 1368.5(1)$ pm, $c = 912.8(1)$ pm, wR2 = 0.1113, 2102 F^2 values, 65 variables for $Tb_{0.980(4)}PdIn_{2.020(4)}$; and $a = 1358.8(1)$ pm, $c = 908.4(1)$ pm, wR2 = 0.0777, 1983 F^2 values, 64 variables for $Tm_{0.986(2)}PdIn_{2.014(2)}$. The terbium and thulium compounds show a small homogeneity range where the Tb3/Tm3 position shows mixed occupancy with indium. Again, the palladium and indium atoms form a three-dimensional $[PdIn_2]$ network, but is more complex when compared with that of $LaPdIn_2$. The four crystallographically different rare earth metal atoms lie in larger voids formed by this network. The magnetic and electrical transport properties of $REPdIn_2$ (RE = Pr, Nd, Sm, Gd, Er, Tm, and Lu) have been studied over wide ranges of temperature and magnetic field. All these indides except for $LuPdIn_2$ show localized magnetism due to the presence of magnetic moments on the RE^{3+} ions. The compounds with RE = Pr, Nd, Sm, and Gd order magnetically at low temperatures. $PrPdIn_2$ is antiferromagnetic below $T_N = 5.5$ K. The other three phases show complex magnetic behavior below $T_N = 4.9$, 9, and 10 K, for $NdPdIn_2$, $SmPdIn_2$, and $GdPdIn_2$, respectively. In the case of $GdPdIn_2$ the magnetic ordering involves a strong ferromagnetic component. For $SmPdIn_2$ another phase transition at $T_t = 5.5$ K has been established, probably a change in the magnetic structure. In contrast to the other compounds, $ErPdIn_2$ and $TmPdIn_2$ remain Curie−Weiss paramagnetic down to 1.7 K, and $LuPdIn_2$ is a Pauli paramagnet. All the compounds studied show metallic conductivity with some features characteristic of crystal field interactions and/or spin fluctuations. The magnetic phase transitions in $PrPdIn_2$, $NdPdIn_2$, $SmPdIn_2$, and $GdPdIn_2$ manifest themselves as distinct anomalies in the temperature-dependent resistivity. In the ordered state the resistivity shows a behavior reflecting reduction in the spin-disorder scattering.

Introduction

Recent investigations of the ternary alkaline earth metal (AE)−transition metal (T)−indium and tin systems revealed a large family of intermetallic compounds $AETIn_2$ (AE = Ca, Sr, Ba; T = Ni, Cu, Rh, Pd, Ir, Pt, Au)[1−5] and $CaTSn_2$ (T = Rh, Pd, Ir).[6] The structural chemistry and chemical bonding of these indides and stannides can easily be understood on the basis of the Zintl−Klemm concept. These intermetallics crystallize with the orthorhombic $MgCuAl_2$-type structure (space

* To whom correspondence should be addressed. E-mail: pottgen@uni-muenster.de.
[†] E-mail: vazar@franko.lviv.ua.
[‡] E-mail: dkaczor@int.pan.wroc.pl.

10.1021/cm031139m CCC: $27.50
Published on Web 01/13/2004

group *Cmcm*),[7] an ordered variant of the well-known Re$_3$B type.[8] The indium and tin substructures strongly resemble the structure of a hexagonal diamond, lonsdaleite,[9] and they can be considered as orthorhombically distorted networks of the indium substructure of the hexagonal Zintl phases CaIn$_2$ and SrIn$_2$.[10] Here, the calcium and strontium atoms transfer their valence electrons to the indium atoms. The latter thus obtain the electron count of the fourth main group and consequently form a three-dimensional tetrahedral network. If we introduce late transition metals into these structures, the T atoms tend to fill their d bands. Since the alkaline earth metal atoms have already transferred their valence electrons to the indium network, d-band filling is only possible through an oxidation of the indium network. In the AETIn$_2$ indides, the In−In distances are longer than those in the binary Zintl phases. The electronegative transition metal atoms are located within distorted triangles formed by the alkaline earth metal atoms.

The AETIn$_2$ and AETSn$_2$ compounds show some flexibility for the electron count. Besides a change of the transition metal component, it is also possible to substitute the divalent alkaline earth metals by divalent or trivalent rare earth metal (RE) atoms. So far, the isotypic compounds RENiIn$_2$ (RE = Eu−Dy),[1,11] REPdIn$_2$ (RE = Ce, Eu, Yb),[12,13] RERhIn$_2$,[14−16] and EuIrSn$_2$[17] have been reported.

Our search for further isotypic intermetallics revealed a variety of compounds with similar composition but different structures. In CaRhIn$_2$ and CaIrIn$_2$[18] the indium substructures are similar, but due to the lower electron count, we observe a different distortion of the networks, leading to a different space group. A peculiar situation occurs in the RENiIn$_2$ series. Here, the MgCuAl$_2$-type structure forms only with RE = Y, Eu, Gd−Dy.[1,11] With the larger rare earth metals cerium, praseodymium, neodymium, and samarium a new structure type occurs,[19,20] which derives from the MgCuAl$_2$ type by chemical twinning. For SrAuSn$_2$ we observed a totally different atomic arrangement. This structure shows a modulation that results from different tilting of Sn$_2$ dumbbells.[21]

Table 1. Lattice Parameters of Tetragonal Indides REPdIn$_2$ with HfNiGa$_2$-Type Structure

compound	*a*/pm	*c*/pm	*V*/nm^3
YPdIn$_2$	1369.5(2)	912.4(2)	1.7112
PrPdIn$_2$	1397.7(1)	925.5(1)	1.8080
NdPdIn$_2$	1391.9(1)	922.42(9)	1.7871
SmPdIn$_2$	1388.3(1)	918.6(1)	1.7705
GdPdIn$_2$	1376.5(1)	915.6(1)	1.7348
TbPdIn$_2$	1368.5(1)	912.8(1)	1.7095
DyPdIn$_2$	1368.6(1)	912.1(1)	1.7084
HoPdIn$_2$	1365.6(1)	911.0(1)	1.6989
ErPdIn$_2$	1362.1(1)	910.0(1)	1.6883
TmPdIn$_2$	1358.8(1)	908.4(1)	1.6772
LuPdIn$_2$	1353.7(1)	906.9(1)	1.6619

We have now extended our investigations with respect to the REPdIn$_2$ compounds. So far, only the cerium,[12] europium, and ytterbium[13] compound are known. Our studies revealed the new isotypic compound LaPdIn$_2$, but with praseodymium, neodymium, samarium, and the late rare earth metals we observed the non-centrosymmetric HfNiGa$_2$-type structure,[22,23] which has so far only been observed for ZrTGa$_2$ and HfTGa$_2$ (T = Co, Ni). The synthesis and structure refinements of the new REPdIn$_2$ compounds are reported herein. Besides the crystal chemistry we also investigated the magnetic and electrical properties of these exciting materials. Preliminary results of this work have recently been presented at a conference.[24]

Experimental Procedures

Synthesis. Starting materials for the syntheses of the REPdIn$_2$ indides were ingots of the rare earth metals (Johnson Matthey), palladium powder (Degussa-Hüls, 200 mesh), and indium tear drops (Johnson Matthey), all with stated purities better than 99.9%. In a first step the larger rare earth metal ingots were cut into smaller pieces and arc-melted[25] to small buttons (ca. 200 mg) under an argon atmosphere. The argon was purified over silica gel, molecular sieves, and titanium sponge (900 K). The rare earth metal buttons were then mixed with cold-pressed pellets (∅ 6 mm) of palladium powder and pieces of the indium tear drops in the ideal 1:1:2 atomic ratio and arc-melted under an argon pressure of 600 mbar. The samples were remelted three times to achieve homogeneity. Subsequently, the buttons were sealed in evacuated silica tubes and annealed at 870 K for 1 month. This procedure resulted in pure polycrystalline samples.

For single-crystal growth a different annealing procedure was used. The samples with praseodymium, terbium, and thulium were crushed and powdered in a steel mortar and cold-pressed to pellets of 6-mm diameter. The pellets were placed in small tantalum containers and sealed in evacuated silica

(1) Zaremba, V. I.; Zakharko, O. Ya.; Kalychak, Ya. M.; Bodak, O. I. *Dopov. Akad. Nauk Ukr. RSR, Ser. B* **1987**, 44.
(2) Sysa, L. V.; Kalychak, Ya. M. *Crystallogr. Rep.* **1993**, *38*, 278.
(3) Hoffmann, R.-D.; Pöttgen, R.; Landrum, G. A.; Dronskowski, R.; Künnen, B.; Kotzyba, G. *Z. Anorg. Allg. Chem.* **1999**, *625*, 789.
(4) Hoffmann, R.-D.; Rodewald, U. Ch.; Pöttgen, R. *Z. Naturforsch.* **1999**, *54b*, 38.
(5) Hoffmann, R.-D.; Pöttgen, R. *Chem. Eur. J.* **2001**, *7*, 382.
(6) Hoffmann, R.-D.; Kuβmann, D.; Rodewald, U. Ch.; Pöttgen, R.; Rosenhahn, C.; Mosel, B. D. *Z. Naturforsch.* **1999**, *54b*, 709.
(7) Aronsson, B.; Bäckmann, M.; Rundqvist, S. *Acta Chem. Scand.* **1960**, *14*, 1001.
(8) Perlitz, H.; Westgren, A. *Ark. Kemi, Miner. Geol.* **1943**, *16B*, 1.
(9) Donohue, J. *The Structures of the Elements*; Wiley: New York, 1974.
(10) Iandelli, A. *Z. Anorg. Allg. Chem.* **1964**, *330*, 221.
(11) Kalychak, Ya. M.; Galadzhun, Ya. V. *Z. Kristallogr.* **1997**, *212*, 292.
(12) Ijiri, Y.; DiSalvo, F. J.; Yamane, H. *J. Solid State Chem.* **1996**, *122*, 143.
(13) Galadzhun, Ya. V.; Hoffmann, R.-D.; Kotzyba, G.; Künnen, B.; Pöttgen, R. *Eur. J. Inorg. Chem.* **1999**, 975.
(14) Pöttgen, R.; Kuβmann, D. *Z. Anorg. Allg. Chem.* **2001**, *627*, 55.
(15) Hoffmann, R.-D.; Pöttgen, R.; Zaremba, V. I.; Kalychak, Ya. M. *Z. Naturforsch.* **2000**, *55b*, 834.
(16) Zaremba, V. I.; Dubenskiy, V. P.; Pöttgen, R. *Z. Naturforsch.* **2002**, *57b*, 798.
(17) Pöttgen, R.; Hoffmann, R.-D.; Möller, M. H.; Kotzyba, G.; Künnen, B.; Rosenhahn, C.; Mosel, B. D. *J. Solid State Chem.* **1999**, *145*, 174.
(18) Hoffmann, R.-D.; Pöttgen, R. *Z. Anorg. Allg. Chem.* **2000**, *626*, 28.
(19) Zaremba, V. I.; Kalychak, Ya. M.; Dubenskiy, V. P.; Hoffmann, R.-D.; Pöttgen, R. *J. Solid State Chem.* **2000**, *152*, 560.
(20) Zaremba, V. I.; Kalychak, Ya. M.; Tyvanchuk, Yu. B.; Hoffmann, R.-D.; Möller, M. H.; Pöttgen, R. *Z. Naturforsch.* **2002**, *57b*, 791.
(21) Esmaeilzadeh, S.; Hoffmann, R.-D.; Pöttgen, R., unpublished results.
(22) Markiv, V. Ya.; Belyavina, N. N.; Zavodnik, V. E. *Dopov. Akad. Nauk. Ukr. RSR, Ser. B* **1988**, 51.
(23) Schlüter, M.; Heying, B.; Pöttgen, R. *Z. Naturforsch.* **2003**, *58b*, 16.
(24) Zaremba, V. I.; Rodewald, U. Ch.; Hoffmann, R.-D.; Pöttgen, R. *Z. Kristallogr.* **2003**, *Suppl. 20*, 160.
(25) Pöttgen, R.; Gulden, Th.; Simon, A. *GIT Labor-Fachzeitschrift* **1999**, *43*, 133.

Table 2. Crystal Data and Structure Refinement for $LaPdIn_2$, $PrPdIn_2$, $Tb_{0.980(4)}PdIn_{2.020(4)}$, and $Tm_{0.986(2)}PdIn_{2.014(2)}$

empirial formula	$LaPdIn_2$	$PrPdIn_2$	$Tb_{0.980(4)}PdIn_{2.020(4)}$	$Tm_{0.986(2)}PdIn_{2.014(2)}$
molar mass	474.95 g/mol	476.95 g/mol	494.01 g/mol	504.21 g/mol
lattice parameters	see text	Table 1	Table 1	Table 1
formula units per cell	$Z = 4$	$Z = 20$	$Z = 20$	$Z = 20$
space group	*Cmcm* (No. 63)	*I*4*mm* (No. 107)	*I*4*mm* (No. 107)	*I*4*mm* (No. 107)
calculated density	8.48 g/cm^3	8.76 g/cm^3	9.60 g/cm^3	9.98 g/cm^3
crystal size	$28 \times 75 \times 100\ \mu m^3$	$35 \times 85 \times 160\ \mu m^3$	$30 \times 75 \times 120\ \mu m^3$	$35 \times 80 \times 95\ \mu m^3$
transmission (max : min)	2.37	2.05	2.47	2.70
absorption coefficient	28.0 mm^{-1}	30.4 mm^{-1}	38.3 mm^{-1}	44.5 mm^{-1}
detector distance	60	60 mm	60 mm	
exposure time	21 min	8 min	12 min	
ω range; increment	0−180°, 1.0°	0−180°, 1.0°	0−180°, 1.0°	
integr. parameters A, B, EMS	15.9, 2.5, 0.026	15.0, 4.0, 0.016	14.0, 4.0, 0.024	
$F(000)$	804	4060	4173	4254
θ range	3−35°	3−35°	4−35°	2−35°
range in *hkl*	±7, ±17, ±11	±22, ±22, ±14	±21, ±21, ±14	±24, ±24, 0−12
total no. reflections	2234	13401	12786	8227
independent reflections	393 ($R_{int} = 0.0695$)	2102 ($R_{int} = 0.0376$)	2079 ($R_{int} = 0.1316$)	1983 ($R_{int} = 0.0736$)
reflections with $I > 2\sigma(I)$	380 ($R_{sigma} = 0.0327$)	2098 ($R_{sigma} = 0.0173$)	2019 ($R_{sigma} = 0.0641$)	1654 ($R_{sigma} = 0.0590$)
data/restraints/parameters	380/0/16	2102/1/64	2079/1/65	1983/1/64
goodness-of-fit on F^2	1.347	1.019	1.143	1.071
final R indices [$I > 2\sigma(I)$]	R1 = 0.0411	R1 = 0.0195	R1 = 0.0400	R1 = 0.0375
	wR2 = 0.0894	wR2 = 0.0662	wR2 = 0.1102	wR2 = 0.0733
R indices (all data)	R1 = 0.0451	R1 = 0.0195	R1 = 0.0412	R1 = 0.0539
	wR2 = 0.1149	wR2 = 0.0662	wR2 = 0.1113	wR2 = 0.0777
extinction coefficient	0.015(4)	0.0046(1)	0.00087(6)	0.00203(6)
twin ratio; BASF		0.44(2)	0.39(2)	
Flack parameter				0.01(1)
largest diff. peak and hole	2.08 and −2.51 e/Å^3	2.94 and −1.54 e/Å^3	3.87 and −3.88 e/Å^3	4.37 and −4.39 e/Å^3

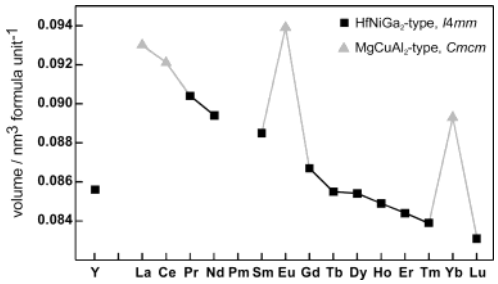

Figure 1. Plot of the cell volumes of the $REPdIn_2$ indides per formula unit. The data for the cerium,[12] europium, and ytterbium[13] compounds were taken from the literature and plotted for comparison.

tubes, which were placed in a muffle furnace. The furnace was first heated at 1250 K ($PrPdIn_2$), respectively 1275 K ($TbPdIn_2$ and $TmPdIn_2$), within 20 h and held at those temperatures for 12 h. The cooling procedure was similar for the three indides: at a rate of 5 K/h to 1070 K, at 10 K/h to 400 K, and finally at 50 K/h to room temperature. The samples could easily be separated from the tantalum crucibles.

The $LaPdIn_2$ crystals were grown from an indium flux. The arc-melted $LaPdIn_2$ samples were crushed, powdered, and pressed to a pellet. The latter was sealed in a tantalum tube together with small pieces of indium in the ratio $LaPdIn_2$:In of 1:2. The tantalum tube was further sealed in a silica ampule to prevent oxidation and first annealed at 1220 K for 3 days. Subsequently, the tube was cooled to room temperature at a rate of 5 K/h. Well-shaped single crystals of $LaPdIn_2$ could be isolated from the indium flux.

For both synthesis techniques no reactions of the samples with the crucible material could be detected. Polycrystalline samples and powders are stable in moist air. No deterioration was observed after several months. Single crystals exhibit metallic luster and powders are dark gray. The samples were investigated by EDX analyses using a Leica 420 I scanning electron microscope. The measured compositions were all close to the ideal value. No impurity elements could be detected.

Structural Characterization. The samples were routinely characterized through Guinier powder patterns using Cu Kα_1 radiation and α-quartz ($a = 491.30$ pm, $c = 540.46$ pm) as an internal standard. To ensure correct indexing, the observed patterns were compared with calculated ones,[26] taking the positions of the refined structures. The refined lattice parameters are listed in Table 1. The lattice parameters for orthorhombic $LaPdIn_2$ are $a = 463.79(7)$ pm, $b = 1074.3(2)$ pm, $c = 746.4(2)$ pm, and $V = 0.3719$ nm^3. A plot of the cell volumes per formula unit is presented in Figure 1. $EuPdIn_2$ and $YbPdIn_2$ show the expected positive deviation from the smooth curve due to the divalent character of the rare earth element. The terbium compound shows a slightly smaller cell volume as expected, most likely indicating a small region of homogeneity, as indicated by the structure refinement. Nevertheless, the cell parameters of the single crystal and the powder agreed very well.

Small irregularly shaped single crystals were isolated from the annealed samples of $LaPdIn_2$, $PrPdIn_2$, $TbPdIn_2$, and $TmPdIn_2$. They were thoroughly investigated on a Buerger precession camera equipped with an imaging plate system (Fujifilm BAS-1800) to establish both symmetry and suitability for intensity data collection.

Intensity data of $TmPdIn_2$ were recorded at room temperature by use of a four-circle diffractometer (CAD4) with graphite monochromatized Mo Kα radiation ($\lambda = 71.073$ pm) and a scintillation counter with pulse-height discrimination. The scans were taken in the $\omega/2\theta$ mode and empirical absorption corrections were applied on the basis of psi-scan data. The data sets for $LaPdIn_2$, $PrPdIn_2$, and $TbPdIn_2$ were collected on a Stoe IPDS-II diffractometer with graphite monochromatized Mo Kα radiation. All relevant crystallographic data for the data collections and evaluations are listed in Table 2.

The isotypy of $LaPdIn_2$ with $MgCuAl_2$, space group *Cmcm*, and the corresponding alkaline earth transition metal indides was already evident from the Buerger photographs. The positions of $CaPdIn_2$[3] were taken as starting parameters for the least-squares refinement. A systematic investigation of the $PrPdIn_2$, $TbPdIn_2$, and $TmPdIn_2$ data sets revealed only the systematic extinctions for a body-centered lattice, leading to the possible space groups *I*4/*mmm*, *I*4*mm*, *I*$\bar{4}$2*m*, and *I*$\bar{4}$*m*2. The atomic sites of $PrPdIn_2$, $TbPdIn_2$, and $TmPdIn_2$ were determined from automatic interpretations of direct methods

(26) Yvon, K.; Jeitschko, W.; Parthé, E. *J. Appl. Crystallogr.* **1977**, *10*, 73.

Table 3. Atomic Coordinates and Equivalent Isotropic Displacement Parameters for LaPdIn$_2$, PrPdIn$_2$, Tb$_{0.980(4)}$PdIn$_{2.020(4)}$, and Tm$_{0.986(2)}$PdIn$_{2.014(2)}$

atom	Wyckoff position	*x*	*y*	*z*	U_{eq}[a]
		LaPdIn$_2$ (MgCuAl$_2$ Type; *Cmcm*)			
La	4c	0	0.07546(7)	1/4	108(3)
Pd	4c	0	0.70764(10)	1/4	113(3)
In	8f	0	0.36051(6)	0.05128(10)	112(3)
		PrPdIn$_2$ (HfNiGa$_2$ Type; *I*4*mm*)			
Pr1	8d	0.71950(2)	0	0.61820(5)	87(1)
Pr2	8c	0.70325(2)	*x*	0.63088(4)	88(1)
Pr3	2a	0	0	0.01276(9)	99(1)
Pr4	2a	0	0	0.54244(9)	98(1)
Pd1	8d	0.78208(4)	0	0.97650(7)	112(1)
Pd2	8c	0.66014(3)	*x*	0.96880(7)	100(1)
Pd3	4b	0	1/2	0.88810(11)	126(1)
In1	16e	0.85917(2)	0.64726(2)	0.88008(5)	97(1)
In2	8d	0.83413(4)	0	0.28644(7)	107(1)
In3	8d	0.61702(4)	0	0.14024(7)	111(1)
In4	8c	0.86651(3)	*x*	0.78597(6)	104(1)
		Tb$_{0.980(4)}$PdIn$_{2.020(4)}$ (HfNiGa$_2$ Type; *I*4*mm*)			
Tb1	8d	0.28082(5)	0	0.38270(7)	93(1)
Tb2	8c	0.29731(3)	*x*	0.37003(7)	92(1)
Tb3[b]	2a	0	0	0.98378(16)	103(4)
Tb4	2a	0	0	0.45450(16)	119(2)
Pd1	8d	0.21416(9)	0	0.02161(13)	117(2)
Pd2	8c	0.33955(5)	*x*	0.02834(12)	94(2)
Pd3	4b	0	1/2	0.11120(19)	116(3)
In1	16e	0.14188(5)	0.35125(5)	0.12087(9)	99(1)
In2	8d	0.16463(8)	0	0.71249(12)	102(2)
In3	8d	0.38223(7)	0	0.86026(12)	109(2)
In4	8c	0.13208(6)	*x*	0.21736(11)	105(2)
		Tm$_{0.986(2)}$In$_{2.014(2)}$ (HfNiGa$_2$ Type; *I*4*mm*)			
Tm1	8d	0.71969(4)	0	0.61596(7)	77(1)
Tm2	8c	0.70247(3)	*x*	0.62953(8)	78(1)
Tm3[b]	2a	0	0	0.01831(15)	84(3)
Tm4	2a	0	0	0.54518(15)	90(2)
Pd1	8d	0.78704(7)	0	0.98048(14)	90(2)
Pd2	8c	0.66085(5)	*x*	0.97374(13)	73(2)
Pd3	4b	0	1/2	0.8906(2)	97(2)
In1	16e	0.85776(4)	0.64971(4)	0.87842(10)	79(1)
In2	8d	0.83601(6)	0	0.28803(12)	78(1)
In3	8d	0.61752(6)	0	0.14086(12)	89(2)
In4	8c	0.86944(5)	*x*	0.78153(12)	84(1)

[a] U_{eq} (pm^2) is defined as one-third of the trace of the orthogonalized $\mathbf{U}_{ij}$ tensor. [b] These positions were refined with a mixed occupancy: Tb3 (80(4)% Tb + 20(4)% In) and Tm3 (86(2)% Tm + 14(2)% In).

with SHELXS-97[27] in the non-centrosymmetric space group *I*4*mm*. From the preliminary refinement cycles the Pearson code *tI*80 was readily evident. With that Pearson code the HfNiGa$_2$ structure, space group *I*4*mm*, is listed in Pearson's Handbook.[28] We observed similar atomic positions; however, a clear site assignment was not possible since the nickel−gallium ordering was not determined in the original work.[22] On the basis of the interatomic distances and refinements of the occupancy parameters, a clear palladium−indium ordering was evident for the praseodymium crystal. This work motivated a reinvestigation of the HfNiGa$_2$ structure. In a recent paper[23] we reported on the nickel−gallium ordering in that compound. In the subsequent refinement cycles for the PrPdIn$_2$, TbPdIn$_2$, and TmPdIn$_2$ data sets, the transition metal−p element ordering of the new HfNiGa$_2$ refinement was used.

The structures were then successfully refined with anisotropic displacement parameters using SHELXL-97[29] (full-matrix least-squares on F^2). As a check for the correct compositions, the occupancy parameters were varied in separate series of least-squares cycles along with the displacement parameters. All sites were fully occupied within three standard deviations for LaPdIn$_2$ and PrPdIn$_2$, and in the final cycles the ideal composition was assumed. The Tb3 and Tm3 occupancy parameters of TbPdIn$_2$ and TmPdIn$_2$ significantly deviated from full occupancy. A smaller scattering power was detected for these two positions. As is known from other thulium−nickel−indides,[30] mixing of the rare earth metal with indium is possible and most likely accounts for the deviations observed here. In the final cycles, the Tb3 and Tm3 positions were refined with mixed Tb3/In and Tm3/In occupancies as listed in Table 3.

Subsequent difference Fourier syntheses revealed no significant residual peaks. Refinement of the Flack parameter[31,32] gave no indication of twinning by inversion for TmPdIn$_2$, while the Flack parameters of the praseodymium and the terbium compound were close to 0.5. The inversion twin matrix was introduced and these two structures were refined again as inversion twins. All relevant details concerning the refine-

Table 4. Interatomic Distances (pm) in the Structures of LaPdIn$_2$ and PrPdIn$_2$[a]

					LaPdIn$_2$					
La:	1	Pd	304.1	Pd:	2	In	278.5	In:	1	Pd	278.5
	2	Pd	328.7		4	In	284.8		2	Pd	284.8
	4	In	330.3		1	La	304.1		1	In	296.6
	2	In	340.3		2	La	328.7		1	In	309.3
	4	In	359.3		2	La	399.3		2	La	330.3
	2	Pd	399.3						1	La	340.3
	2	La	406.9						2	In	340.6
									2	La	359.3
					PrPdIn$_2$					
Pr1:	2	Pd2	312.3	Pd1:	1	In3	276.0	In2:	2	Pd2	280.4
	2	In4	318.0		2	In4	282.6		1	Pd1	295.9
	2	In1	321.0		2	In1	286.7		2	Pr2	322.7
	2	In1	328.2		1	In2	295.9		2	In2	327.9
	1	Pd1	343.0		1	Pr3	306.4		1	Pr4	331.5
	1	In2	346.3		2	Pr2	318.7		1	In3	332.2
	2	In3	348.3		1	Pr1	343.0		1	Pr3	343.4
	1	Pd3	373.5	Pd2:	2	In2	280.4		1	Pr1	346.3
	1	Pd3	395.6		2	In1	290.6		2	In1	350.2
	1	Pr4	398.3		1	In4	298.2	In3:	1	Pd1	276.0
	2	Pr2	415.6		1	Pr2	308.9		1	Pd3	281.7
Pr2:	1	Pd2	308.9		2	Pr1	312.3		1	Pd3	285.0
	2	Pd1	318.7		1	Pr4	323.8		2	In1	304.5
	2	In2	322.7		1	Pr2	324.1		2	In1	313.9
	1	Pd2	324.1	Pd3:	2	In3	281.7		1	In3	327.1
	2	In1	324.3		4	In1	284.9		1	In2	332.3
	2	In1	326.8		2	In3	285.0		2	Pr1	348.3
	1	In4	347.7		2	Pr1	373.5		2	Pr2	379.3
	1	In4	353.2		2	Pr1	395.6	In4:	2	Pd1	282.6
	2	In3	379.3	In1:	1	Pd3	284.9		1	Pd2	298.2
	2	Pr1	415.6		1	Pd1	286.7		2	Pr1	318.0
	1	Pr3	416.4		1	Pd2	290.6		2	In1	318.8
Pr3:	4	Pd1	306.4		1	In3	304.5		1	Pr3	337.2
	4	In4	337.2		1	In3	313.9		1	Pr4	347.0
	4	In2	343.4		1	In4	318.8		1	Pr2	347.7
	4	Pr2	416.4		1	Pr1	321.0		1	Pr2	353.2
	1	Pr4	435.3		1	Pr2	324.3		2	In4	373.2
Pr4:	4	Pd2	323.8		1	Pr2	326.8				
	4	In2	331.5		1	Pr1	328.2				
	4	In4	347.0		1	In2	350.2				
	4	Pr1	398.3								
	1	Pr3	435.3								

[a] All distances of the first coordination spheres are listed. Standard deviations are all equal to or less than 0.2 pm.

(27) Sheldrick, G. M. *SHELXS-97, Program for Crystal Structure Refinement*; University of Göttingen: Göttingen, Germany, 1997.
(28) Villars, P.; Calvert, L. D. *Pearson's Handbook of Crystallographic Data for Intermetallic Phases*, 2nd ed. and desk ed.; ASM International: Materials Park, OH, 1991 and 1997.
(29) Sheldrick, G. M. SHELXL-97, Program for Crystal Structure Refinement, University of Göttingen, Germany, 1997.
(30) Lukachuk, M.; Kalychak, Ya. M.; Pöttgen, R.; Hoffmann, R.-D. *Z. Kristallogr.* **2003**, *Suppl. 20*, 142.
(31) Flack, H. D.; Bernadinelli, G. *Acta Crystallogr.* **1999**, *A55*, 908.
(32) Flack, H. D.; Bernadinelli, G. *J. Appl. Crystallogr.* **2000**, *33*, 1143.

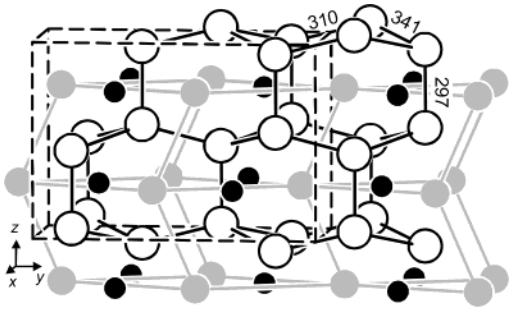

Figure 2. Cutout of the $LaPdIn_2$ structure. The lanthanum, palladium, and indium atoms are drawn as gray, filled, and open circles, respectively. The distorted trigonal lanthanum prisms and the indium network are emphasized. Selected bond lengths are given in pm.

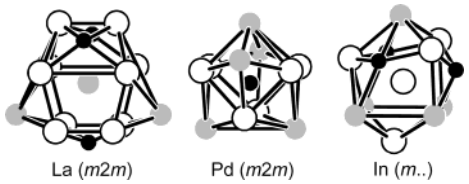

Figure 3. Coordination polyhedra in the $LaPdIn_2$ structure. The site symmetries are given in parentheses.

ments are listed in Table 2. Atomic coordinates and interatomic distances are given in Tables 3 and 4. Listings of the anisotropic displacement parameters and the structure factors are available.[33]

Physical Property Investigations. The magnetic susceptibility and magnetization of $REPdIn_2$ (RE = Pr, Nd, Sm, Gd, Er, Tm and Lu) were measured on single polycrystalline pieces (~100 mg mass) of each compound in the temperature range 1.72−400 K and in magnetic fields up to 5 T, employing a Quantum Design MPMS-5 SQUID magnetometer. For electrical transport measurements bar-shaped samples of typical dimensions 0.3 × 0.3 × 5 mm^3 were cut from the annealed arc-melted buttons using a wire saw. Electrical contacts were made by spot-welding gold wires. The current leads were additionally fixed to the specimen's surface by silver epoxy. The electrical resistivity was measured in the temperature range 4.2−300 K (down to 1.6 K for $PrPdIn_2$) using a conventional four-point dc technique. Furthermore, for $NdPdIn_2$, $SmPdIn_2$, and $GdPdIn_2$ the isothermal field dependence of the resistivity was studied at T = 4.2, 6, and 8 K.

Results and Discussion

Crystal Chemistry and Chemical Bonding. Twelve new $REPdIn_2$ indides have been synthesized and some of the structures have been refined from single-crystal diffractometer data. With the large rare earth metals lanthanum and cerium, the $REPdIn_2$ compounds adopt the orthorhombic $MgCuAl_2$ structure.[7] The geometrical motif of that structure, that is, palladium-centered trigonal prisms, has already been given by Ijiri et al. for $CePdIn_2$.[12] A perspective view of the $LaPdIn_2$ structure is presented in Figure 2; the coordination polyhedra are shown in Figure 3. As discussed in detail in previous manuscripts,[4,5] the structure is best described as a palladium-filled substructure, $LaIn_2$, which resembles the well-known Zintl phase $CaIn_2$;[10] however, such

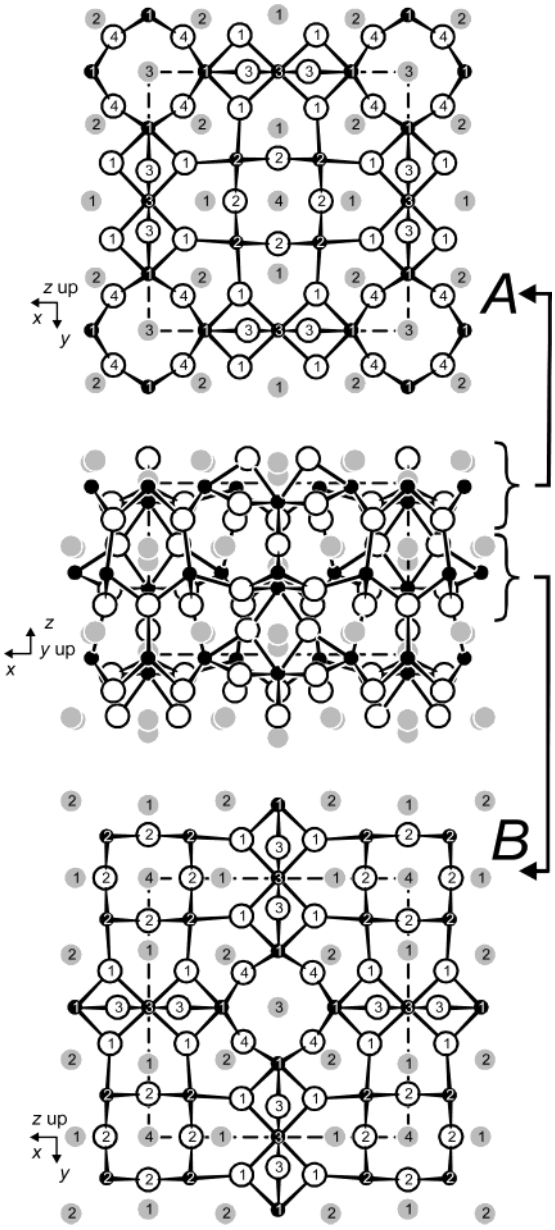

Figure 4. Crystal structure of $PrPdIn_2$. In the middle a view of the structure along the y axis is presented. The complex structure contains the layers A (around z = 0) and B (around z = $^1/_2$). Both layers have the same composition. Due to the body-centered lattice, they are shifted by $^1/_2$, $^1/_2$, $^1/_2$. Praseodymium, palladium, and indium atoms are drawn as gray, filled, and open circles, respectively.

structures are not known with trivalent cations since in a Zintl−Klemm formulation, $Ca^{2+}[In^-]_2$, we cannot account for the surplus electron of lanthanum. In the ternary compound $LaPdIn_2$ this arrangement is realized in a distorted manner. From an electronic viewpoint, the more electronegative palladium atoms tend to fill their d bands and therefore account for the surplus electron of lanthanum. This model of chemical bonding was discussed in detail for the isotypic alkaline earth metal compounds.[3−6]

The Pd−In distances in $LaPdIn_2$ range from 279 to 285 pm, close to the sum of the covalent radii of 278 pm for palladium and indium.[34] The Pd−In interactions

(33) Details may be obtained from: Fachinformationszentrum Karlsruhe, D-76344 Eggenstein-Leopoldshafen (Germany), by quoting the Registry No's. CSD-413448 ($LaPdIn_2$), CSD-413449 ($PrPdIn_2$), CSD-413450 ($TbPdIn_2$), and CSD-413451 ($TmPdIn_2$). E-mail: crysdata@fiz-karlsruhe.de.

(34) Emsley, J. *The Elements*, 3rd ed.; Oxford University Press: Oxford, 1999.

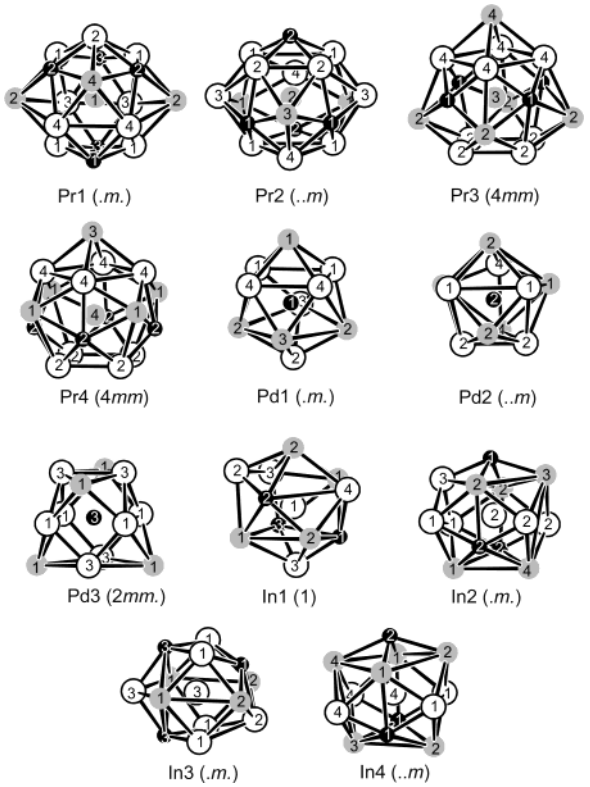

Figure 5. Coordination polyhedra in the PrPdIn$_2$ structure. All neighbors listed in Table 3 are shown. Single digit numbers correspond to the atom designations. The site symmetries are given in parentheses.

can be considered as the strongest ones in the structure. The indium atoms within the indium substructure of LaPdIn$_2$ have one neighbor at 297 pm, one at 309 pm, and two more distant ones at 341 pm. Considering the In−In distances in the tetragonal body-centered indium,[9] where each indium atom has four nearest indium neighbors at 325 pm and eight further neighbors at 338 pm, the shorter ones in LaPdIn$_2$ can certainly be considered as strongly bonding. The lengths of the In−In bonds strongly depend on the electron count per formula unit and the nature of the transition metal. In that view LaPdIn$_2$ is similar to the gold-containing compounds. The trends in In−In bond lengths within the indium substructures of MgCuAl$_2$ intermetallics are discussed in a recent paper.[15] For further details concerning the MgCuAl$_2$ intermetallics we refer to our previous manuscripts.[1−6,11,13−18]

With praseodymium and the smaller rare earth elements, the REPdIn$_2$ indides crystallize with the tetragonal HfNiGa$_2$ structure.[22,23] As a first comparison of these tetragonal structures with the orthorhombic structures of LaPdIn$_2$ and CePdIn$_2$, we plot the cell volumes per formula unit in Figure 1. As expected from the lanthanoid contraction, the cell volumes decrease from the lanthanum to the lutetium compound. CePdIn$_2$[12] shows no deviation from the plot, in agreement with trivalent cerium, as is evident also from the magnetic data. Large positive deviations occur for EuPdIn$_2$ and YbPdIn$_2$ reflecting the divalent europium and ytterbium. This is consistent with the magnetic data listed in ref 13.

As an example for the tetragonal compounds, we present a projection of the PrPdIn$_2$ structure in Figure

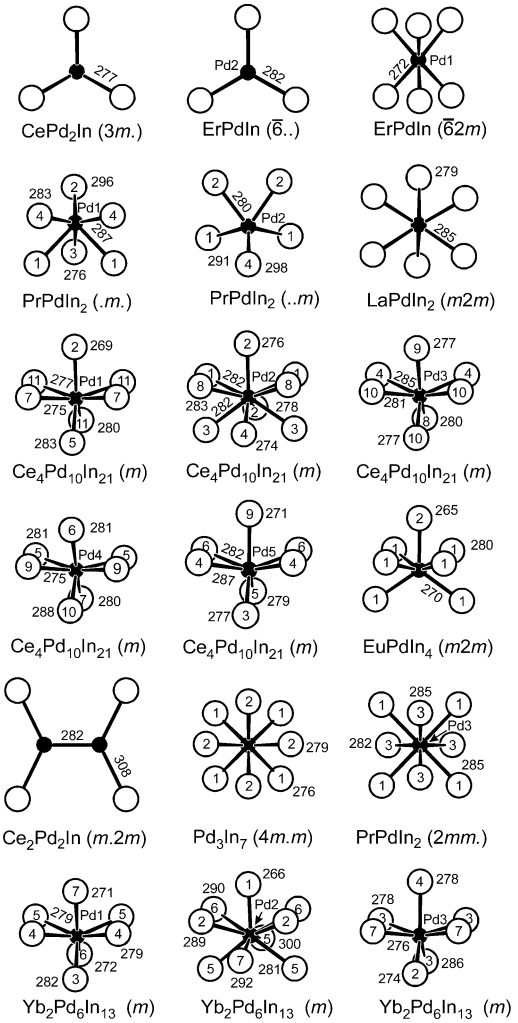

Figure 6. Cutouts of PdIn$_x$ ($x = 3-9$) units in various ternary rare earth palladium indides and in Pd$_3$In$_7$. The palladium and indium atoms are drawn as black and open circles, respectively. Relevant interatomic distances and atom labels are indicated. The site symmetries are given in parentheses. Note that the rare earth metal atoms are omitted for clarity.

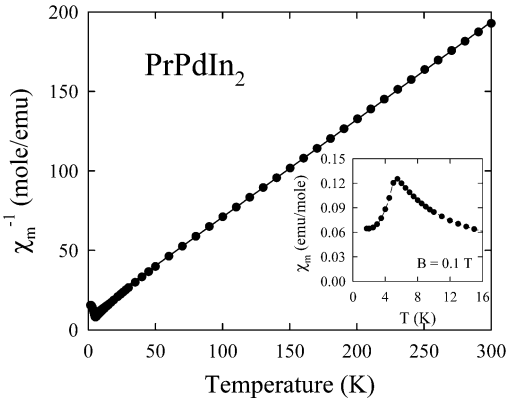

Figure 7. Temperature dependence of the reciprocal molar magnetic susceptibility of PrPdIn$_2$. The solid line is a Curie−Weiss fit with the parameters given in the text. Inset: low-temperature magnetic susceptibility measured in a field of 0.1 T.

4. The structure is composed of two different layers A (around $z = 0$) and B (around $z = {}^1/_2$) as outlined in that figure. Both layers have the same composition. Due to the body-centered Bravais lattice, the A layer is shifted by ${}^1/_2$, ${}^1/_2$, ${}^1/_2$ with respect to the B layer. The layers are

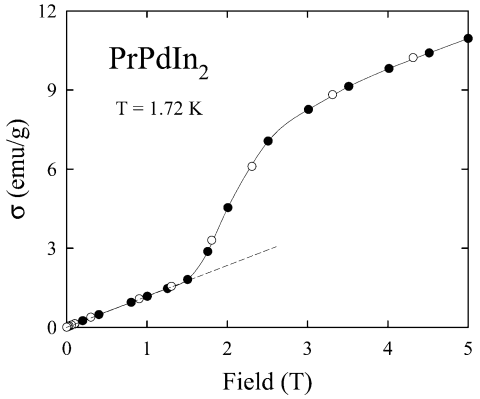

Figure 8. Field variation of the magnetization in $PrPdIn_2$ taken at 1.72 K with increasing (full circles) and decreasing (open circles) magnetic field. The dashed line emphasizes the straight-line behavior of $\sigma(B)$ below the metamagnetic phase transition.

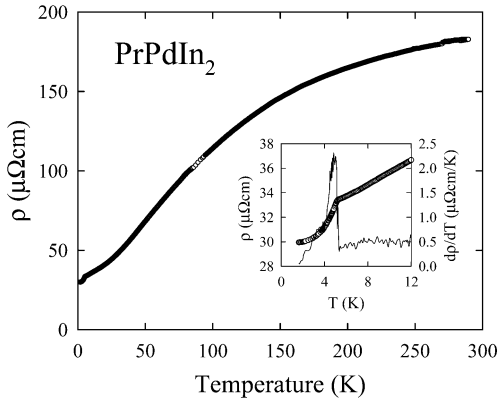

Figure 9. Temperature dependence of the electrical resistivity of $PrPdIn_2$. Inset: low-temperature resistivity (symbols) and temperature derivative of the resistivity (solid line).

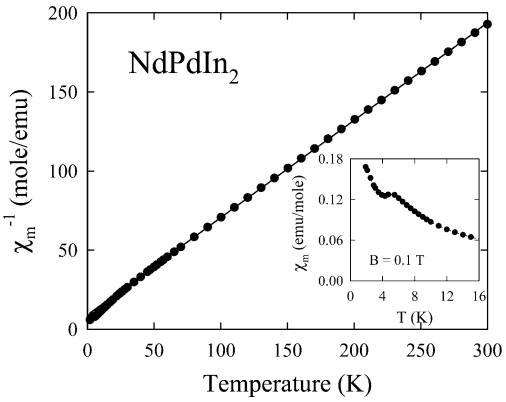

Figure 10. Temperature dependence of the reciprocal molar magnetic susceptibility of $NdPdIn_2$. The solid line is a Curie–Weiss fit with the parameters given in the text. Inset: low-temperature magnetic susceptibility measured in a field of 0.1 T.

condensed via Pd–In bonds forming a complex three-dimensional network.

The three crystallographically different palladium atoms have between five and eight indium neighbors at Pd–In distances ranging from 276 to 298 pm, similar to $LaPdIn_2$ discussed above. The range of In–In distances from 305 to 373 pm, however, is much larger than that in the lanthanum compound. The shorter ones of these In–In interactions can be considered as bonding. The Pd1 and Pd2 atoms both have coordination

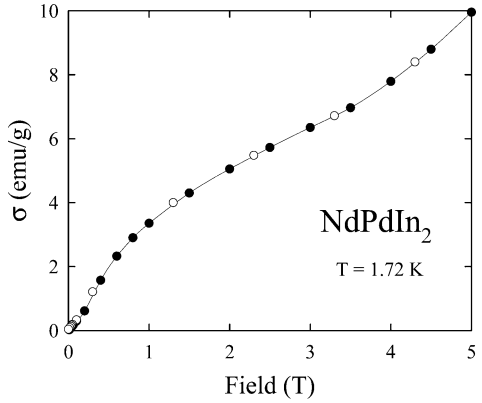

Figure 11. Field variation of the magnetization in $NdPdIn_2$ taken at 1.72 K with increasing (full circles) and decreasing (open circles) magnetic field.

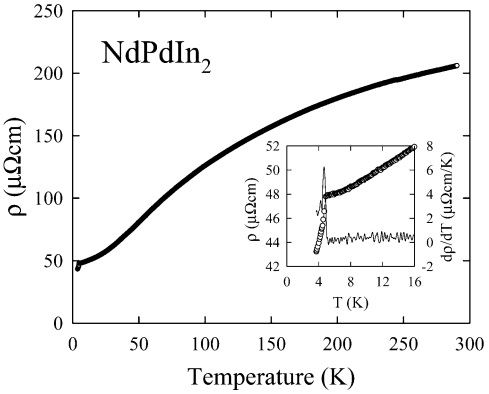

Figure 12. Temperature dependence of the electrical resistivity of $NdPdIn_2$. Inset: low-temperature resistivity (symbols) and temperature derivative of the resistivity (solid line).

number (CN) 10, that is, 6 In + 4 Pr for Pd1 and 5 Pd + 5 Pr for Pd2. The situation is different for Pd3, which has eight nearest indium neighbors. The coordination number is increased by four praseodymium atoms at the longer Pr–Pd distances of 374 and 396 pm. These four palladium atoms certainly complete the coordination shell of Pd3, but the Pr–Pd contacts may only be considered as weakly bonding.

The praseodymium atoms are located in different cages within the complex three-dimensional $[PdIn_2]$ network. The coordination numbers are 17 for Pr1, Pr2, Pr3, and Pr4 (Figure 5). The lanthanum atoms in $LaPdIn_2$ have the same coordination number.

Finally, it is interesting to discuss the various $PdIn_x$ units in the palladium-based indides. In Figure 6 we present the monomeric units observed in the structures of $CePd_2In$,[35] ErPdIn,[36] $PrPdIn_2$, $LaPdIn_2$, $Ce_4Pd_{10}In_{21}$,[37] $EuPdIn_4$,[15] Ce_2Pd_2In,[38] Pd_3In_7,[39] and $Yb_2Pd_6In_{23}$.[40] The coordination numbers by indium range from 3 to 9.

(35) Xue, B.; Hulliger, F.; Bärlocher, C.; Estermann, M. *J. Alloys Compd*. **1993**, *191*, L9.
(36) Zaremba, V. I.; Hoffmann, R.-D.; Pöttgen, R., unpublished results.
(37) Zaremba, V. I.; Rodewald, U. Ch.; Kalychak, Ya. M.; Galadzhun, Ya. V.; Kaczorowski, D.; Hoffmann, R.-D.; Pöttgen, R. *Z. Anorg. Allg. Chem*. **2003**, *629*, 434.
(38) Giovannini, M.; Michor, H.; Bauer, E.; Hilscher, G.; Rogl, P.; Ferro, R. *J. Alloys Compd*. **1998**, *280*, 26.
(39) Häussermann, U.; Elding-Ponten, M.; Svensson, Ch.; Lidin, S. *Chem. Eur. J*. **1998**, *4*, 1007.
(40) Zaremba, V. I.; Dubenskiy, V. P.; Kalychak, Ya. M.; Hoffmann, R.-D.; Pöttgen, R. *Solid State Sci*. **2002**, *4*, 1293.

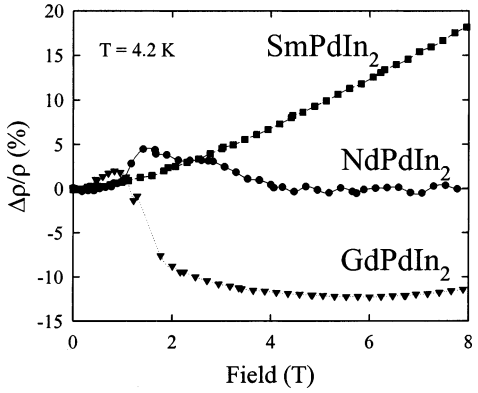

Figure 13. Field variation of the transverse magnetoresistivity of NdPdIn$_2$, SmPdIn$_2$, and GdPdIn$_2$ measured at 4.2 K.

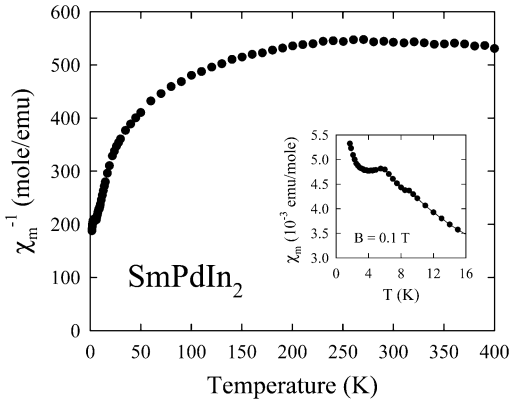

Figure 14. Temperature dependence of the reciprocal molar magnetic susceptibility of SmPdIn$_2$. Inset: low-temperature magnetic susceptibility measured in a field of 0.1 T.

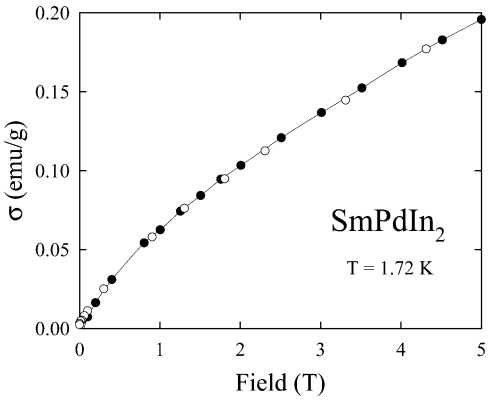

Figure 15. Field variation of the magnetization in SmPdIn$_2$ taken at 1.72 K with increasing (full circles) and decreasing (open circles) magnetic field.

Those palladium atoms with a low indium coordination number certainly have more rare earth metal atoms in their coordination shell. The various Pd−In distances cover the large range from 265 to 296 pm. Most of these Pd−In distances compare well with the sum of the covalent radii of 278 pm.[34] The structures are built up from a condensation of these units via In−In bonds or by palladium atoms sharing common indium neighbors. A special situation occurs for the Mo_2FeB_2-type structure of Ce_2Pd_2In,[38] where the palladium atoms have also a palladium neighbor at a Pd−Pd distance of 282 pm. This peculiar bonding situation is certainly due to the low indium content. All other structures have no close Pd−Pd contacts.

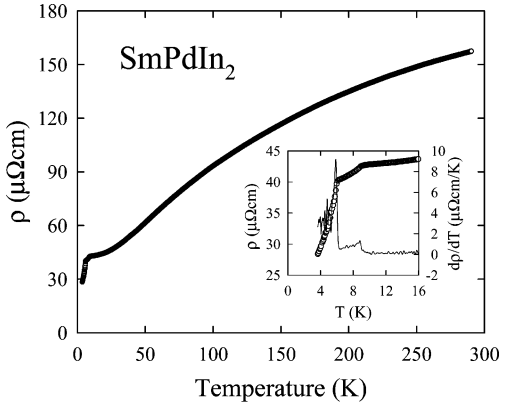

Figure 16. Temperature dependence of the electrical resistivity of SmPdIn$_2$. Inset: low-temperature resistivity (symbols) and temperature derivative of the resistivity (solid line).

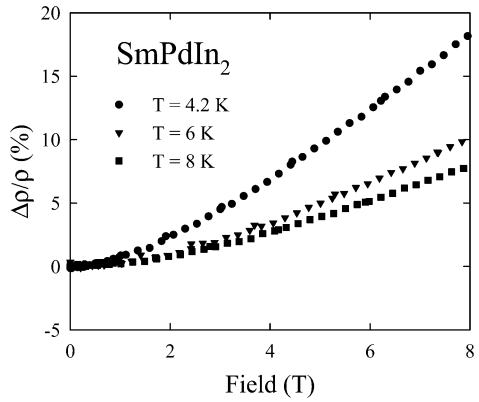

Figure 17. Field variation of the transverse magnetoresistivity of SmPdIn$_2$ measured at 4.2, 6, and 8 K.

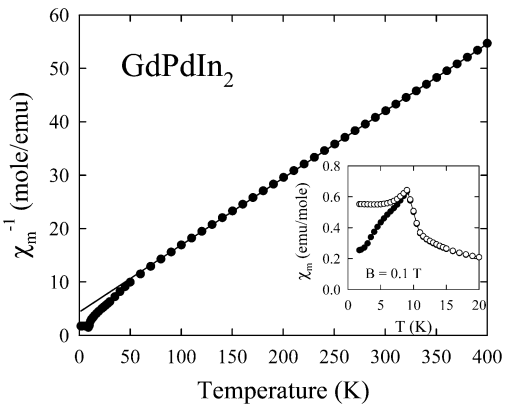

Figure 18. Temperature dependence of the reciprocal molar magnetic susceptibility of GdPdIn$_2$. The solid line is a Curie−Weiss fit with the parameters given in the text. Inset: low-temperature magnetic susceptibility measured in a field of 0.1 T in zero-field-cooling (filled circles) and field-cooling (open circles) mode.

Physical Properties. *PrPdIn$_2$.* The temperature-dependent reciprocal magnetic susceptibility of PrPdIn$_2$ is shown in Figure 7. Above about 30 K, $\chi^{-1}(T)$ follows a Curie−Weiss (CW) law with an effective magnetic moment $\mu_{eff} = 3.61(2)\ \mu_B$ and a paramagnetic Curie temperature $\Theta_p = -15.7(3)$ K. At lower temperatures some deviation from the straight-line behavior is observed, presumably due to crystal field effects. The experimental value of μ_{eff} is nearly equal to that characteristic of a free Pr^{3+} ion (3.58 μ_B), while the negative Θ_p hints for the presence of antiferromagnetic

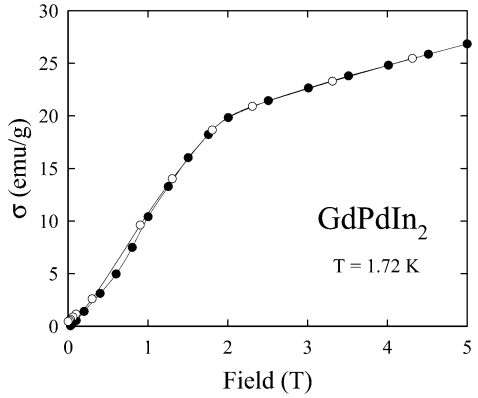

Figure 19. Field variation of the magnetization in $GdPdIn_2$ taken at 1.72 K with increasing (full circles) and decreasing (open circles) magnetic field.

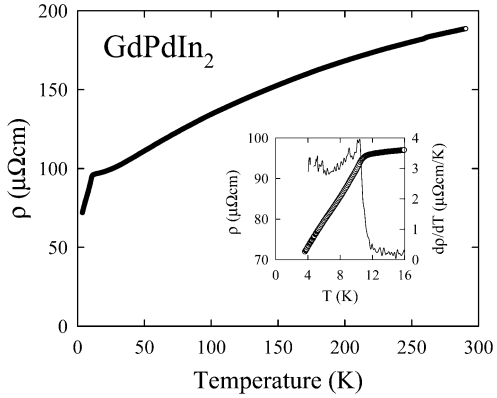

Figure 20. Temperature dependence of the electrical resistivity of $GdPdIn_2$. Inset: low-temperature resistivity (symbols) and temperature derivative of the resistivity (solid line).

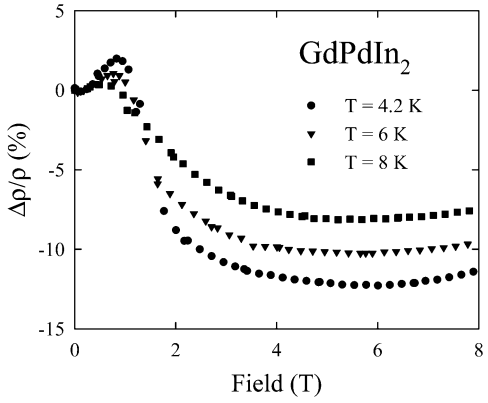

Figure 21. Field variation of the transverse magnetoresistivity of $GdPdIn_2$ measured at 4.2, 6, and 8 K.

exchange interactions. Indeed, as seen from the inset of Figure 7, $PrPdIn_2$ orders antiferromagnetically at T_N = 5.5(2) K. Further evidence for long-range antiferromagnetic ordering at low temperatures comes from the field-dependent behavior of the magnetization measured at 1.72 K (Figure 8) that shows a linear increase with rising field up to the critical value B_c = 1.5(2) T, above which a pronounced metamagnetic-like transition occurs.

The electrical resistivity of $PrPdIn_2$ behaves in a manner characteristic of magnetic metals (Figure 9). The strongly curved $\rho(T)$ may be attributed to spin fluctuations, which probably involve d electrons of both

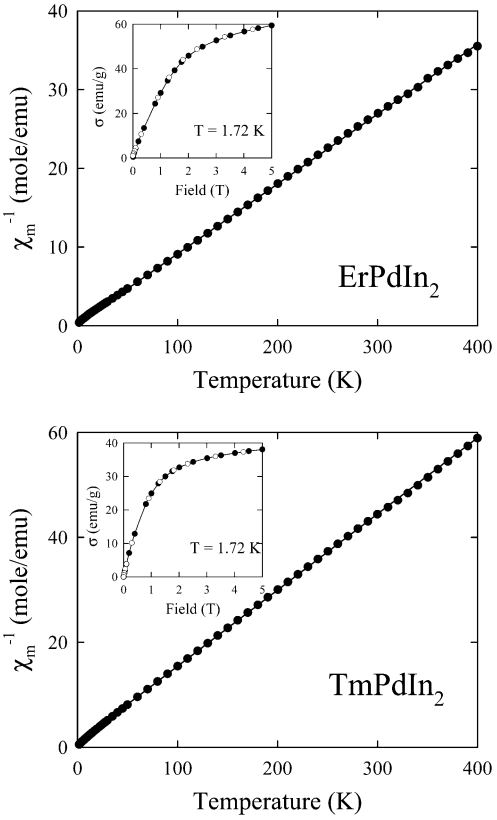

Figure 22. Temperature dependence of the reciprocal molar magnetic susceptibility of $ErPdIn_2$ (top) and $TmPdIn_2$ (bottom). The solid lines are Curie−Weiss fits with the parameters given in the text. Insets: field variations of the magnetization taken at 1.72 K with increasing (full circles) and decreasing (open circles) magnetic field.

Pr and Pd atoms. The magnetic phase transition manifests itself as a distinct kink in $\rho(T)$ at T_N = 5.5(1) K and a sharp maximum at this temperature in the temperature derivative of the resistivity (see the inset to Figure 9).

$NdPdIn_2$. The magnetic properties of $NdPdIn_2$ are summarized in Figures 10 and 11. The CW behavior of the magnetic susceptibility is observed down to 30 K with the least-squares fit parameters: μ_{eff} = 3.61(3) μ_B (i.e., equal to the theoretical Nd^{3+} ion value of 3.62 μ_B) and Θ_p = −14.7(3) K. At T_N = 4.9(2) K, the $\chi(T)$ curve shows a peak (inset of Figure 10) that may be interpreted as the fingerprint of antiferromagnetism. At lower temperatures, however, the susceptibility exhibits a steep upturn and this feature, together with a sigmoid-like shape of the field variation of the magnetization at 1.72 K (Figure 11), implies that the magnetic behavior in $NdPdIn_2$ is quite complex.

As displayed in Figure 12, $NdPdIn_2$ shows metallic conductivity. The $\rho(T)$ dependence is curvilinear, likely due to crystal field interactions and spin fluctuations. At the onset of the ordered state the resistivity drops rapidly, mainly due to a large reduction in the spin-disorder scattering. This effect results in the occurrence of a spiky maximum at T_N in the temperature variation of the temperature derivative of the resistivity (inset of Figure 12). Upon application of a magnetic field, the resistivity measured at 4.2 K first slightly increases but above about 1.7 T it tends to come back to its zero field value, which is reached near 4 T and kept constant in

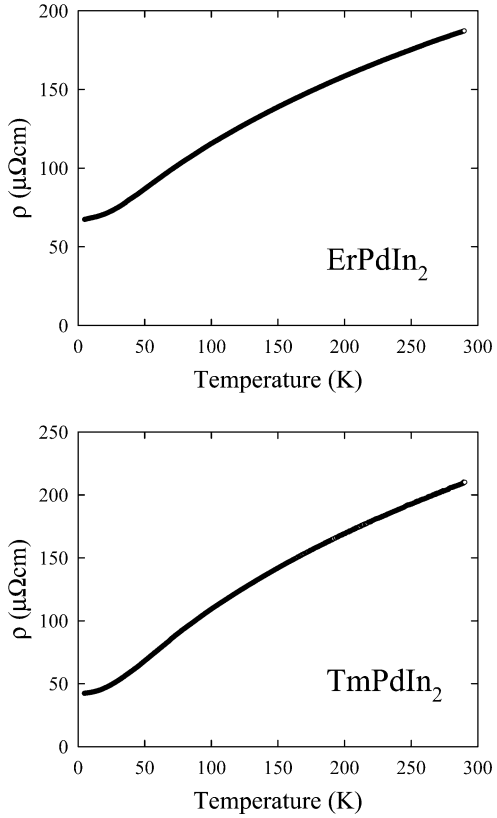

Figure 23. Temperature dependence of the electrical resistivity of $ErPdIn_2$ (top) and $TmPdIn_2$ (bottom).

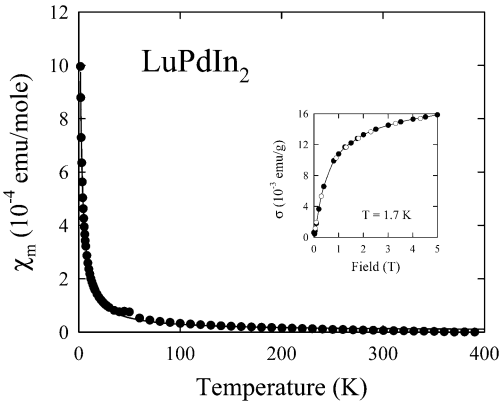

Figure 24. Temperature dependence of the molar magnetic susceptibility of $LuPdIn_2$. The solid line is a fit described in the text. Insets: field variation of the magnetization taken at 1.7 K with increasing (full circles) and decreasing (open circles) magnetic field.

higher fields. This behavior is shown in Figure 13, in the form of the magnetoresistivity isotherm

$$\frac{\Delta\rho}{\rho}(B) = \frac{\rho(B) - \rho(0)}{\rho(0)}$$

$SmPdIn_2$. In the entire temperature range studied, the magnetic susceptibility of this material does not follow the Curie−Weiss law (Figure 14), as frequently found for samarium compounds due to the closeness of the $^6H_{5/2}$ and $^6H_{7/2}$ terms in the Sm^{3+} ground multiplet. Moreover, the susceptibility of $SmPdIn_2$ is remarkably small. There are two peaklike anomalies in $\chi(T)$ occurring at $T_N = 9.0(4)$ K and $T_t = 5.5(2)$ K, which may be associated with magnetic phase transitions: antiferro-

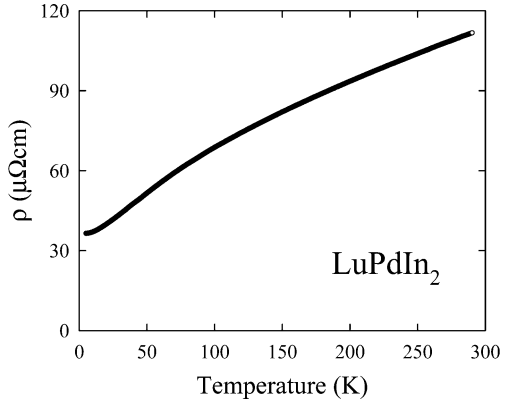

Figure 25. Temperature dependence of the electrical resistivity of $LuPdIn_2$.

magnetic and spin reorientation, respectively. However, below T_t the susceptibility rises with decreasing temperature, and the magnetization taken at 1.72 K (Figure 15) does not vary with magnetic field in a manner expected for simple antiferromagnets. These findings might indicate that the magnetic ground state in $SmPdIn_2$ is probably quite complex.

The two magnetic phase transitions are clearly perceived as kinks in the low-temperature dependence of the resistivity and maxima in its temperature derivative (inset of Figure 16). In the paramagnetic region $\rho(T)$ is curvilinear, probably mainly because of thermal population of crystal field levels in the ground and excited terms. The transverse magnetoresistivity measured in the ordered state is positive and varies roughly as B^2 (Figure 17). At 4.2 K it reaches about 18% in a field of 8 T. With increasing temperature the effect of magnetic field on the resistivity diminishes.

$GdPdIn_2$. In this case the Curie−Weiss behavior of the magnetic susceptibility is observed above 70 K (Figure 18) with the experimental effective magnetic moment $\mu_{eff} = 7.98(2)\ \mu_B$ being in agreement with the value corresponding to Gd^{3+} ions (7.94 μ_B). At lower temperatures there occurs notable deviation from straight-line behavior of $\chi^{-1}(T)$, which might be attributed to short-range magnetic interactions. The latter probably have antiferromagnetic character, as the paramagnetic Curie temperature is strongly negative ($\Theta_p = -35(1)$ K). At first glance, the maximum in $\chi(T)$ corroborates the expectation of antiferromagnetic ordering at low temperatures, yet its unusual shape and distinct dependence of the susceptibility below the peak temperature on the magnetic history of the sample (note the zero-field-cooled and field-cooled curves in the inset of Figure 18) contradict a picture of simple antiferromagnetism. Furthermore, a complex magnetic structure in $GdPdIn_2$, apparently with a ferromagnetic component, can be deduced from the field variation of the magnetization at 1.72 K (Figure 19).

Like the compounds considered above, the gadolinium-based phase shows metallic resistivity of the order of 100−200 $\mu\Omega$·cm at room temperature (Figure 20). At the magnetic phase transition $\rho(T)$ exhibits a kink that results in a sharp maximum in the temperature derivative of the resistivity (inset of Figure 20). In the paramagnetic state $\rho(T)$ is curvilinear, probably mainly because of Mott-Jones-type scattering of the conduction electrons. The transverse magnetoresistivity

measured at 4.2 K is positive in weak magnetic fields, shows a maximum of about 2% near 0.8 T, and subsequently decreases and becomes negative in stronger fields, reaching ca. −12% above 3 T (Figure 21). With rising temperature the absolute magnitude of $\Delta\rho/\rho$ gradually decreases.

$ErPdIn_2$ and $TmPdIn_2$. These two compounds reveal similar magnetic properties characterized by a Curie−Weiss behavior of the magnetic susceptibility and lack of any magnetic phase transition down to the lowest temperature studied (Figure 22). The effective magnetic moment amounts to 9.49(2) and 7.42(3) μ_B for the Er- and Tm-based indide, respectively, in fairly good agreement with the values expected for the respective trivalent ions (9.58 μ_B and 7.56 μ_B, respectively). The paramagnetic Curie temperatures are −2.9(2) and −6.3(2) K, respectively. The magnetization measured at 1.72 K as a function of magnetic field strength behaves in a manner typical for paramagnets, with some curvature toward saturation in high fields (see the insets to Figure 22). The electrical resistivity of both compounds exhibits metallic-type temperature dependencies (Figure 23) with no singularities down to the base temperature.

$LuPdIn_2$. The compound is nonmagnetic, as manifested by a small, nearly temperature-independent magnetic susceptibility (Figure 24) and simple metallic character of the electrical resistivity (Figure 25). The upturn in $\chi(T)$ at low temperatures is most likely caused by paramagnetic impurities in the amount lower than the detectability limit for X-ray powder diffraction. Describing the susceptibility as a sum of a Curie term due to the spurious paramagnetism and a Pauli term accounting for the intrinsic behavior of $LuPdIn_2$ yields the estimates for the latter contribution, $\chi_{TIP} = 4.8 \times 10^{-6}$ emu/mol, and for the Curie parameter, $C = 2.4 \times 10^{-3}$ (K emu)/mol.

Acknowledgment. We thank H.-J. Göcke for the EDX analyses and the Degussa-Hüls AG for a generous gift of palladium powder. Financial support by the Deutsche Forschungsgemeinschaft and by the Fonds der Chemischen Industrie is gratefully acknowledged. V.I.Z. is indebted to the Alexander von Humboldt Foundation for a research stipend.

CM031139M